XVI International Conference on Computational Plasticity. Fundamentals and Applications
COMPLAS 2021
E. Oñate, D. Peric, M. Chiumenti and Eduardo de Souza Neto (Eds)

EVALUATION OF A FRACTURE INDICATOR DEPENDENT ON THE NORMALIZED THIRD INVARIANT OF THE DEVIATORIC STRESS TENSOR AND EQUIVALENT PLASTIC STRAIN

LEONEL L. DELGADO MORALES* **AND LUCIVAL MALCHER†**

* Institute of Industrial Design and Methods (IDMI)
Austral University of Chile
Campus Miraflores, General Lagos 2086, Valdivia, Chile
e-mail: leonel.delgado@uach.cl

† Group of Fatigue Fracture and Materials (GFFM)
University of Brasília
Campus Darcy Ribeiro, Brasília, DF, Brazil
email: malcher@unb.br

Key words: Stress triaxiality, normalized third invariant, ductile fracture indicator, accumulated plastic strain at fracture, AISI 4340 alloy.

Abstract. This work presents a new fracture indicator, which incorporates the effects of the normalized third invariant of the deviatoric stress tensor and the equivalent plastic strain, in its formulation, The proposed indicator is also coupled with the post-processing step of the Gao constitutive model. The tests are applied to specimens manufactured from the AISI 4340 alloy in two heat treatment states. To compare the behavior of the material under different ductility conditions, numerical tests are performed for different stress states. The new fracture indicator presents satisfactory results when observing the forecast of the displacement in the fracture and the levels of reaction force, for the evaluated specimens used in the study.

1 INTRODUCTION

Numerous works present in the literature of the area, the conclusions pointed out that the models mentioned above are not capable of adequately describing the mechanical behavior of a set of materials, since they do not take into account the synergistic effect of important parameters of the stress state, such as stress triaxiality and the third normalized invariant. [1, 2, 3, 4, 5]. Among the most relevant elastoplastic effects, we can highlight the stress triaxiality, in which the hydrostatic stress and the equivalent stress are related. This parameter is related to the control of the size of the elastic regime of the material [6, 7]. From experimental data, it is possible to verify that the stress triaxiality defines the stress state generated in the material. Thus, the ranges of low triaxiality level are established, in which the effects of pure shear and / or combined loading states prevail, and the region of high triaxiality level, in which purely tractive effects predominate. The work developed by Bao [6] presented an important advance in the determination of these effects in ductile materials, correlating the level of plastic deformation in the fracture with the value of the stress triaxiality.

The mechanical behavior of ductile materials in the fracture can be realized considering the

effects of the damage. In this sense, the models based on the Continuous Damage Mechanics (CDM) are an interesting option. The CDM has been widely studied in recent decades, to incorporate new variables into the constitutive model [8]. For Lemaitre and Desmorat [9] the damage represents the creation and growth of micro-cracks, which constitute discontinuities in solid materials, in other words, the damage corresponds to small measurable defects within an elementary representative volume. Vaz Jr. & Owen [10] proposed a ductile fracture indicator based on the damage evolution law presented by Lemaitre [11]. The indicator could be coupled and integrated with the post-processing stage of an elastoplastic model. For Vaz Jr. & Owen [10], the ductile fracture could be determined through the energy released due to the damage and the increase in the equivalent plastic deformation, produced with each increment of total strain.

Recently, several authors have made contributions, in which applications of ductile fracture are described, considering various materials and geometries of specimens. In the proposals by Driemeier et al. [12], Brünig et al. [13], Gerke et al. [14], Yan & Zhao [15] experiments were also carried out with rectangular specimens, reproducing biaxial stress states. Another work of great relevance, developed for materials with very complex behavior, was carried out by Haji Aboutalebi et al. [16], in which experimental tests were carried out for DIN 1623 St12 steel. A significant advance can be found in Farahani et al. [17], whose work published tests on specimens with greater complexity reproducing combined states of tensile and shear in the same test. Brünig et al. [18] and Brünig et al. [19] performed experiments referring to damage and fracture in the negative range of the triaxiality, that is, the effect of compression was considered as a stress state in the evaluation of the behavior of the material. In addition. Brünig [20] presented a numerical model for ductile materials, proposing a formulation that incorporates the damage in the flow function. In this way, plastic strain can be quantified, as well as nucleation and the propagation of micro defects, through the internal damage variable.

This work presents a new ductile fracture indicator, to improve the prediction of material failure. The damage denominator function was modified, which allowed the indicator to be coupled to the post-processing stage of the Gao constitutive model. The results were validated through experimental tests and numerical simulations, using the AISI 4340 alloy [21], a material widely used in the offshore industry, especially in components for the extraction of oil and gas in deep waters. The normalized and annealed alloy was chosen due to the difference in strain levels, to evaluate the fracture indicator, in different stress states and considering the ductility of the alloy. The study presented an analysis for the rectangular specimens, considering the low triaxiality range, to obtain the elastic and plastic characterization of the material. For computer simulations, a finite element academic tool was used. The proposed ductile fracture indicator, coupled with the post-processing step of the Gao model, proves to be quite efficient in the prediction, both for the displacement at fracture and the reaction forces levels.

2 DESCRIPTION OF THE CONSTITUTIVE MODELS

The model based on the Continuous Damage Mechanics, proposed by Lemaitre [11] (see Box 1), and the elastoplastic model published by Gao et al. [4] (see Box 2) are presented below, in a summarized form.

Box 1: Lemaitre mathematical model, with isotropic hardening and isotropic damage

i) Additive decomposition of total strain:

$$\boldsymbol{\varepsilon} = \boldsymbol{\varepsilon}^e + \boldsymbol{\varepsilon}^p$$

ii) Elastic law with damage coupled:

$$\boldsymbol{\sigma} = (1 - D)\mathbb{D}^e : \boldsymbol{\varepsilon}^e$$

iii) Yield function:

$$\phi = \frac{q}{(1-D)} - \sigma_{y_0} - R(r)$$

iv) Plastic flow rule and evolution equation for r e D:

$$\dot{\boldsymbol{\varepsilon}}^P = \dot{\gamma}\boldsymbol{N} = \dot{\gamma}\sqrt{\frac{3}{2}}\frac{\boldsymbol{S}}{\|\boldsymbol{S}\|}\frac{1}{(1-D)}$$

$$\dot{r} = \dot{\gamma}$$

$$\dot{D} = \dot{\gamma}\,\frac{1}{(1-D)}\left(\frac{-Y}{S}\right)^s$$

Where:

$$Y = -\frac{1}{2}\boldsymbol{\varepsilon^e} : \mathbb{D} : \boldsymbol{\varepsilon^e}$$

v) Loading/unloading rule:

$$\dot{\gamma} \geq 0, \qquad \phi \leq 0, \qquad \dot{\gamma}\phi = 0$$

Box 2: Gao mathematical model (simplified), with isotropic hardening

i) Additive decomposition of total strain:

$$\boldsymbol{\varepsilon} = \boldsymbol{\varepsilon}^e + \boldsymbol{\varepsilon}^p$$

ii) Elastic law:

$$\boldsymbol{\sigma} = \mathbb{D}^e : \boldsymbol{\varepsilon}^e$$

iii) Yield function:

$$\phi = c\left(27{J_2}^3 + bJ_3\right)^{\frac{1}{6}} - \sigma_{y0} - H(\bar{\varepsilon}^p)\,\bar{\varepsilon}^p$$

$$c = \left[\frac{4}{728}b + 1\right]^{-\frac{1}{6}}$$

$$\kappa = 27{J_2}^3 + bJ_3$$

iv) Plastic flow rule

$$\dot{\boldsymbol{\varepsilon}}^p \equiv \dot{\gamma}\boldsymbol{N} = \dot{\gamma}\boldsymbol{N} = \dot{\gamma}\left[c\frac{1}{6}(\kappa)^{-\frac{5}{6}}\frac{\partial\kappa}{\partial\boldsymbol{\sigma}}\right]$$

$$\frac{\partial\kappa}{\partial\boldsymbol{\sigma}} = 81{J_2}^2\boldsymbol{S} + \mathrm{b}\det\boldsymbol{S}\left(\boldsymbol{S}^{-T} : \mathbb{I}^d\right)$$

v) Evolution of the accumulated plastic strain:

$$\dot{\bar{\varepsilon}}^p = \dot{\gamma}\frac{\boldsymbol{\sigma} : \boldsymbol{N}}{\sigma_y}$$

vi) Loading/unloading rule:

$$\dot{\gamma} \geq 0, \qquad \phi \leq 0, \qquad \dot{\gamma}\phi = 0$$

3 DEFINITION OF A NEW DUCTILE FRACTURE INDICATOR

Based on the contribution made by Malcher & Mamiya [21] who modified the Lemaitre damage denominator [11] and using the proposal by Vaz Jr & Owen [12] a new fracture indicator was structured. To define a ductile fracture indicator that considers the state of tension and the ductility of the material, the following function is written:

$$I = \int_0^{\bar{\varepsilon}_f^p} \frac{-Y}{\left[S_{1/3}\xi^2 + S_0(1-\xi^2) + \left(S_0 - S_{1/3}\right)\frac{\bar{\varepsilon}^p}{\bar{\varepsilon}_f^p}(1-\xi^2)\right]} d\bar{\varepsilon}^p, \tag{1}$$

where I represents the new ductile fracture indicator, Y is the thermodynamic force associated with damage, $S_{1/3}$ and S_0 represents the denominator of damage calibrated by a cylindrical smooth bar specimen subjected to a pure tensile and pure shear loading condition, respectively, ξ is stress triaxiality, $\bar{\varepsilon}^p$ and $\bar{\varepsilon}_f^p$ is the equivalent plastic strain and the equivalent plastic strain at fracture, respectively.

4 NUMERICAL STRATEGY

An implicit numerical integration algorithm is structured, based on the operator split methodology [22, 23], the pseudo-time discretization is implemented following the implicit Euler schema. The non-linear equations system is solved by the Newton-Raphson method. Box 3, Box 4, Box 5 describes the numerical steps required.

Box 3: Return mapping algorithm Newton-Raphson (Lemaitre).

i) Given the trial stress state as initial step:

$$\boldsymbol{\sigma}_{n+1}^{(0)} = \boldsymbol{\sigma}_n \qquad \Delta\gamma^{(0)} = 0 \qquad D_{n+1}^0 = D_n$$

ii) Solve the system of linearized equation for: $\boldsymbol{\sigma}_{n+1}$, D_{n+1}, $\Delta\gamma$.

$$\begin{bmatrix} \frac{\partial R_{\Delta\gamma}}{\partial \Delta\gamma} & \frac{\partial R_{\Delta\gamma}}{\partial \boldsymbol{\sigma}_{n+1}} & \frac{\partial R_{\Delta\gamma}}{\partial D_{n+1}} \\ \frac{\partial R_{\boldsymbol{\sigma}}}{\partial \Delta\gamma} & \frac{\partial R_{\boldsymbol{\sigma}}}{\partial \boldsymbol{\sigma}_{n+1}} & \frac{\partial R_{\boldsymbol{\sigma}}}{\partial D_{n+1}} \\ \frac{\partial R_D}{\partial \Delta\gamma} & \frac{\partial R_D}{\partial \boldsymbol{\sigma}_{n+1}} & \frac{\partial R_D}{\partial D_{n+1}} \end{bmatrix}^k \cdot \begin{bmatrix} \delta\Delta\gamma \\ \delta\boldsymbol{\sigma}_{n+1} \\ \delta D_{n+1} \end{bmatrix}^{k+1} = -\begin{bmatrix} R_{\Delta\gamma} \\ R_{\boldsymbol{\sigma}_{n+1}} \\ R_{D_{n+1}} \end{bmatrix}^k$$

iii) Update the unknowns of the problem at the iteration k+1:

$$\boldsymbol{\sigma}_{n+1} = \boldsymbol{\sigma}_{n+1}^{(k)} + \delta\boldsymbol{\sigma}_{n+1}^{(k+1)} \qquad \Delta\gamma = \Delta\gamma^{(k)} + \delta\Delta\gamma^{(k+1)}$$

$$D_{n+1} = D_{n+1}^{(k)} + \delta D_{n+1}^{(k)}$$

Update other state variables:

$$R_{n+1} = R_n + \Delta\gamma$$

$$\boldsymbol{\varepsilon}_{n+1}^e = \mathbb{D}^{-1} : \boldsymbol{\sigma}_{n+1}$$

iv) Verify the convergence:

$$\phi = \frac{\sqrt{\frac{3}{2}\boldsymbol{S}_{n+1} : \boldsymbol{S}_{n+1}}}{(1 - D_{n+1})} - \sigma_{y0} - H\mathrm{R_n} - H\Delta\gamma$$

If $|\Phi| \leq tolerance \implies$ End, otherwise return to step ii).

v) End.

Box 4: Return mapping algorithm Newton-Raphson (Gao).

i) Given the trial stress state as initial step, $k:=0$, initial parameters: $\boldsymbol{S}_{n+1}^{(0)} = \boldsymbol{S}_{n+1}^{trial}$, $\Delta\gamma^{(0)} = 0$, $\bar{\varepsilon}^{p}{}_{n+1}{}^{(0)} = \bar{\varepsilon}^{p}{}_{n}$ and residual equations:

ii) $$\begin{bmatrix} R_{\boldsymbol{S}_{n+1}}(\boldsymbol{S}_{n+1}, \Delta\gamma, \bar{\varepsilon}^{p}{}_{n+1}) \\ R_{\Delta\gamma}(\boldsymbol{S}_{n+1}, \Delta\gamma, \bar{\varepsilon}^{p}{}_{n+1}) \\ R_{\bar{\varepsilon}^{p}{}_{n+1}}(\boldsymbol{S}_{n+1}, \Delta\gamma, \bar{\varepsilon}^{p}{}_{n+1}) \end{bmatrix} = \begin{bmatrix} \boldsymbol{S}_{n+1} - \boldsymbol{S}_{n+1}^{trial} + 2G\Delta\gamma\boldsymbol{N}_{n+1} \\ c\left(27{J_2}_{n+1}{}^3 + b{J_3}_{n+1}\right)^{\frac{1}{6}} - \sigma_{y0} - H(\bar{\varepsilon}^{p})\bar{\varepsilon}^{p}{}_{n+1} \\ \bar{\varepsilon}^{p}{}_{n+1} - \bar{\varepsilon}^{p}{}_{n} - \Delta\gamma\frac{\boldsymbol{S}_{n+1}:\boldsymbol{N}_{n+1}}{\sigma_y} \end{bmatrix}$$

iii) Solve the system of equations:

$$\begin{bmatrix} \frac{\partial R_{\boldsymbol{S}_{n+1}}}{\partial \boldsymbol{S}_{n+1}} & \frac{\partial R_{\boldsymbol{S}_{n+1}}}{\partial \Delta\gamma} & \frac{\partial R_{\boldsymbol{S}_{n+1}}}{\partial \bar{\varepsilon}^{p}{}_{n+1}} \\ \frac{\partial R_{\Delta\gamma}}{\partial \boldsymbol{S}_{n+1}} & \frac{\partial R_{\Delta\gamma}}{\partial \Delta\gamma} & \frac{\partial R_{\Delta\gamma}}{\partial \bar{\varepsilon}^{p}{}_{n+1}} \\ \frac{\partial R_{\bar{\varepsilon}^{p}{}_{n+1}}}{\partial \boldsymbol{S}_{n+1}} & \frac{\partial R_{\bar{\varepsilon}^{p}{}_{n+1}}}{\partial \Delta\gamma} & \frac{\partial R_{\bar{\varepsilon}^{p}{}_{n+1}}}{\partial \bar{\varepsilon}^{p}{}_{n+1}} \end{bmatrix}^{k} \cdot \begin{bmatrix} \delta\boldsymbol{S}_{n+1} \\ \delta\Delta\gamma \\ \delta\bar{\varepsilon}^{p}{}_{n+1} \end{bmatrix}^{k+1} = -\begin{bmatrix} R_{\boldsymbol{S}_{n+1}}(\boldsymbol{S}_{n+1}, \Delta\gamma, \bar{\varepsilon}^{p}{}_{n+1}) \\ R_{\Delta\gamma}(\boldsymbol{S}_{n+1}, \Delta\gamma, \bar{\varepsilon}^{p}{}_{n+1}) \\ R_{\bar{\varepsilon}^{p}{}_{n+1}}(\boldsymbol{S}_{n+1}, \Delta\gamma, \bar{\varepsilon}^{p}{}_{n+1}) \end{bmatrix}^{k}$$

New guess for $\boldsymbol{S}_{n+1}$, $\Delta\gamma$ e $\bar{\varepsilon}^{p}{}_{n+1}$**:**

$$\boldsymbol{S}_{n+1}{}^{(k+1)} = \boldsymbol{S}_{n+1}{}^{(k)} + \delta\boldsymbol{S}_{n+1}{}^{(k+1)}; \qquad \Delta\gamma^{(k+1)} = \Delta\gamma^{(k)} + \delta\Delta\gamma^{(k+1)};$$

$$\bar{\varepsilon}^{p}{}_{n+1}{}^{(k+1)} = \bar{\varepsilon}^{p}{}_{n+1}{}^{(k)} + \delta\bar{\varepsilon}^{p}{}_{n+1}{}^{(k+1)};$$

Update variables:

$$\boldsymbol{\varepsilon}_{n+1}^{e} = [\mathbf{D}^{e}]^{-1}{:}\boldsymbol{\sigma}_{n+1}; \quad \boldsymbol{\sigma}_{n+1} = \boldsymbol{S}_{n+1} + p_{n+1}\boldsymbol{I}$$

iv) Verify the convergence: $\widetilde{\Phi} = c\left(27{J_2}_{n+1}{}^3 + b{J_3}_{n+1}\right)^{\frac{1}{6}} - \sigma_{y0} - H(\bar{\varepsilon}^{p})\bar{\varepsilon}^{p}{}_{n+1}$,
if $\left|\widetilde{\Phi}\right| \leq tolerance \Longrightarrow$ End, otherwise return to step ii)

v) End

Box 5: Integration of the ductile fracture indicator

i) Run Box 2 for the Gao model, to determine: S_{n+1}, $\Delta\gamma$ e $\bar{\varepsilon}^{p}{}_{n+1}$

ii) Calculate ξ_{n+1}, according Equation 1 and to determine $f(\xi_{n+1}, \bar{\varepsilon}^{p}{}_{n+1})$:

$$f(\xi_{n+1}, \bar{\varepsilon}^{p}{}_{n+1}) = S_0 - \left(S_0 - S_{1/3}\right){\xi_{n+1}}^2 + \left(S_0 - S_{1/3}\right)\left(\frac{\bar{\varepsilon}^{p}{}_{n+1}}{\bar{\varepsilon}^{p}{}_{f}}\right)\left(1 - {\xi_{n+1}}^2\right)$$

iii) To determine the damage in pseudo-time t_{n+1}

$$I_{(n+1)} = I_{(n)} + \left[\frac{1}{f(\xi_{n+1}, \bar{\varepsilon}^{p}{}_{n+1})}\left(\frac{{q_{n+1}}^2}{6G} + \frac{{p_{n+1}}^2}{2K}\right)\right](\bar{\varepsilon}^{p}{}_{n+1} - \bar{\varepsilon}^{p}{}_{n})$$

iv) End

5 CALIBRATION PROCEDURE

The hardening curve is obtained from the equation proposed by Kleinermann & Ponthot [24], which considers the isotropic hardening of the material from four parameters, mathematically represented by Equation 2:

$$\sigma_y = \sigma_{y0} + \varsigma\bar{\varepsilon}^p + \left(\sigma_\infty - \sigma_{y0}\right)\left(1 - e^{-\delta\bar{\varepsilon}^p}\right), \quad (2)$$

where σ_{y0} is the initial yield strength, $\bar{\varepsilon}^p$ is the equivalent plastic strain and ς, σ_∞ and δ represents the hardening parameters. Table 1 shows the elastic and plastic parameters for the material used in tensile and shear calibrations.

Table 1: Material parameters – normalized and anneled AISI 4340 alloy.

Description	***Symbol***	***Values***	
		Normalized	***Annealed***
		Tensile	***Tensile***
Young's modulus	E [MPa]	199960	206880
Poisson's ratio	υ	0.30	0.30
Initial yield stress	σ_{y0} [MPa]	657.00	449.00
First parameter calibration	ς [MPa]	819.10	568.20
Second parameter calibration	σ_∞ [MPa]	1022.00	747.00
Calibration exponent	δ	51.90	28.90
Damage denominator $\left(S_{1/3}\right)$	S[MPa]	16.65	25.02
Damage expoent	s	1	1
Critical damage	D_c	0.21	0.21

In the calibration of the damage parameters for the ductile fracture indicator, an objective function was established, which considers the critical damage and the fracture displacement for cylindrical smooth bar specimen, subjected to a tensile loading condition, and rectangular specimens, under a pure shear loading condition. The material parameters are listed in Table 2.

Table 2: Parameters for fracture indicator of Vaz Jr. & Owen and new fracture indicator (AISI 4340 alloy).

Description	***Symbol***	***Vaz Jr. & Owen***		***Proposed***	
		Normalized	***Annealed***	***Normalized***	***Annealed***
Parameter of Gao Model	b	-100	-130 and -140	-100	-130 and -140
Damage denominator in tensile calibration	$S_{1/3}$[MPa]	16.65	25.02	16.65	25.02
Damage denominator in shear calibration	S_0 [MPa]	-	-	14.40	62.04
Critical damage	D_c	0.17	0,16	0.17	0.16
Equivalent plastic strain at fracture	$\bar{\varepsilon}^p{}_f$	-	-	0.67	1.20

The optimized set parameters $S_{1/3}$, S_0 and D_c was determined at the moment when the numerically calculated displacement became equal to the experimentally observed displacement and, the maximum calculated damage reaches the level of critical damage, considering the tensile and shear stress states. The multivariable function is defined in Equation 3:

$$g = \left[\sqrt{\left(\frac{D_c - D_{max}}{D_c}\right)^2 + \left(\frac{u_{f\,exp} - u_{f\,num}}{u_{f\,exp}}\right)^2}\right]_{tensile} + \left[\sqrt{\left(\frac{D_c - D_{max}}{D_c}\right)^2 + \left(\frac{u_{f\,exp} - u_{f\,num}}{u_{f\,exp}}\right)^2}\right]_{shear} \tag{3}$$

where D_c is critical damage, D_{max} represents the maximum calculated damage, $u_{f\,exp}$ is the experimental displacement and $u_{f\,num}$ is the numerical displacement.

5 NUMERICAL RESULTS

Below some preliminary results are shown to demonstrate the accuracy of the new ductile fracture indicator, to discuss the values obtained by each model, the numerical and experimental results are compared. Figure 1 shows the perfect agreement of the numerical and experimental values for the smooth cylindrical specimen. The results correspond to the annealed AISI 4340 alloy.

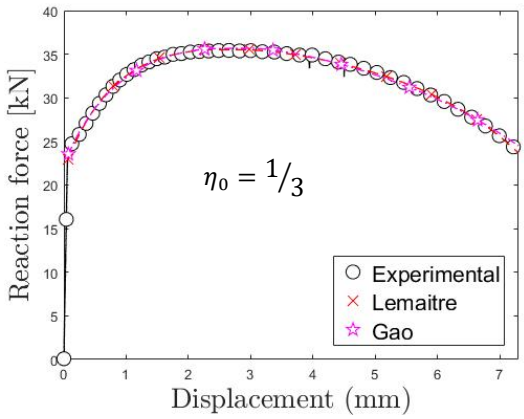

a) Reaction curve - AISI 4340 - annealed

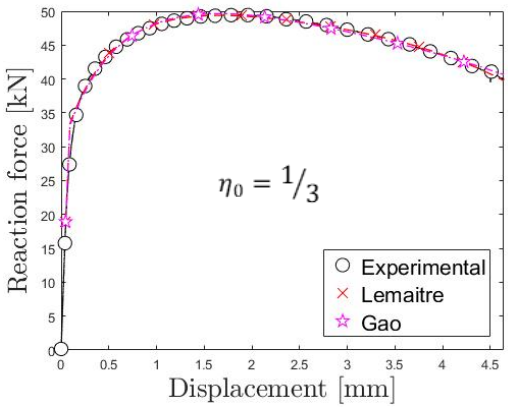

b) Reaction curve - AISI 4340 - normalized

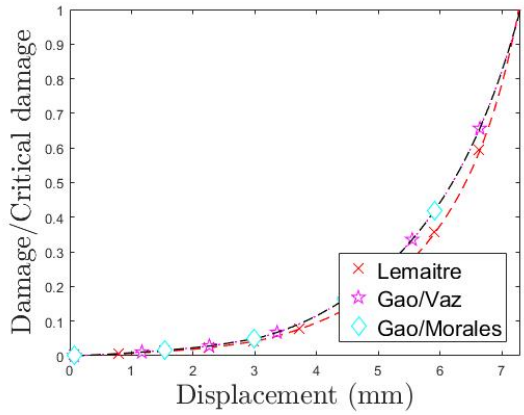

c) Evolution of damage AISI 4340 - annealed

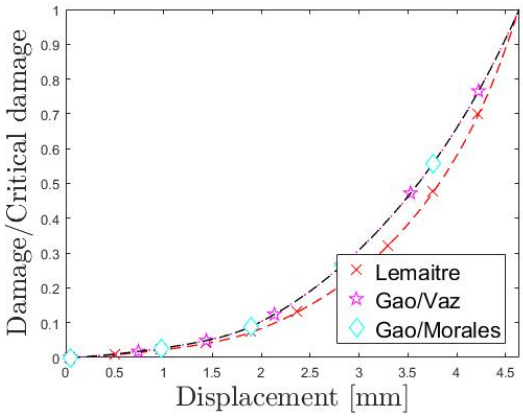

d) Evolution of damage AISI 4340 - normalized

Figure 1: Resoluts cylindrical bar specimens.

Figure 2 shows the damage evolution, as well as the fracture shape for each model used in the study. Observing the cylindrical specimens it is possible to verify that the damage is distributed around the critical point, which coincides with the fracture region of the specimen.

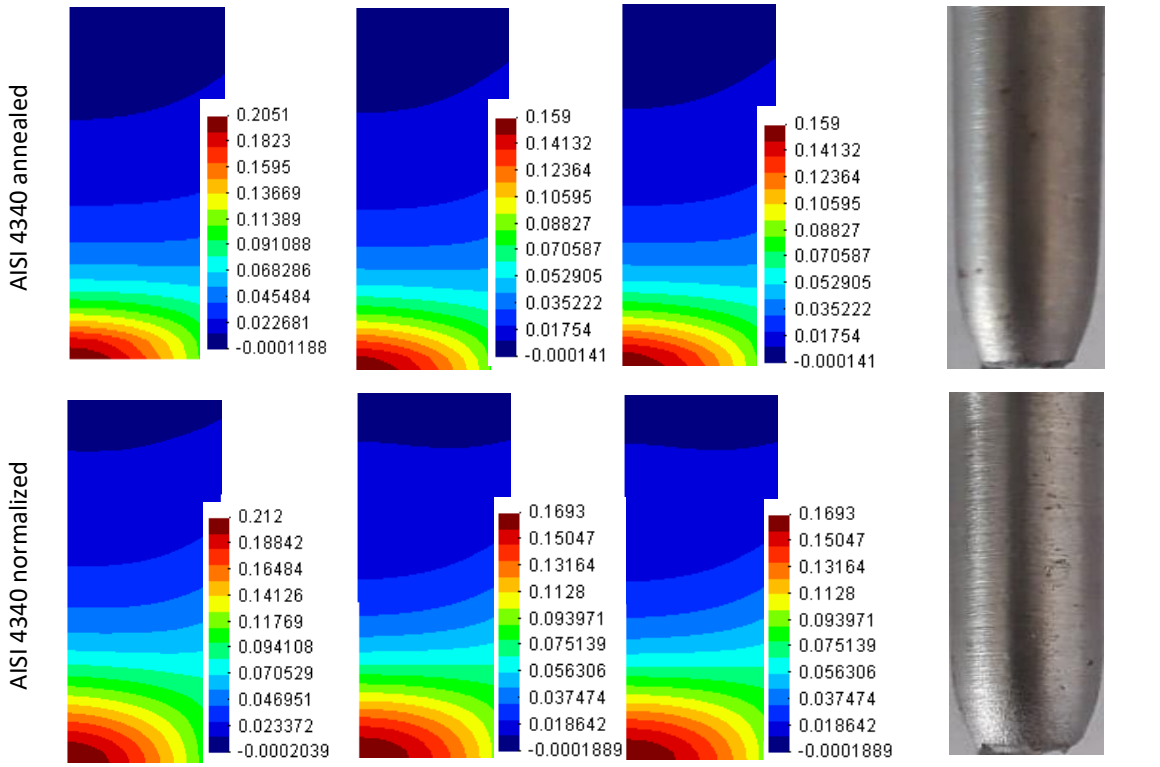

Figure 2: Contour of the damage parameter for cylindrical specimens

The analysis of the ductile fracture indicator was performed for specimens in a stress state within the low-stress triaxiality range. The Lemaitre and Gao models were compared and the results were compared with the damage indicator proposed by Vaz Jr. & Owen [10] and the new ductile fracture indicator. Numerical simulations were performed using the parameters of the Gao model b = -130 and b = -140, for annealed AISI 4340 alloy and b = -100 for normalized AISI 4340 alloy. In Figure 3 (a) and (b) it is possible to verify that the displacement at fracture forecasts and the reaction force improve significantly when using the new ductile fracture indicator for both tested materials. In Figure 3 (c) and (d) it can be seen that the evolution of the incorporated into the Gao model presents a very similar behavior to the Vaz Jr. & Owen [10] indicator. In this study it is also verified that the Lemaitre model makes late or premature predictions of displacement to fracture, depending on the level of ductility material.

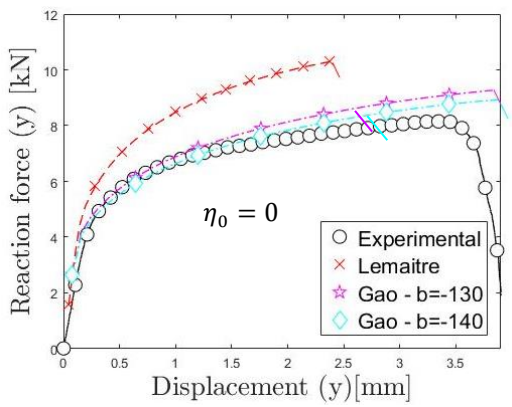

a) Reaction curve - AISI 4340 annealed

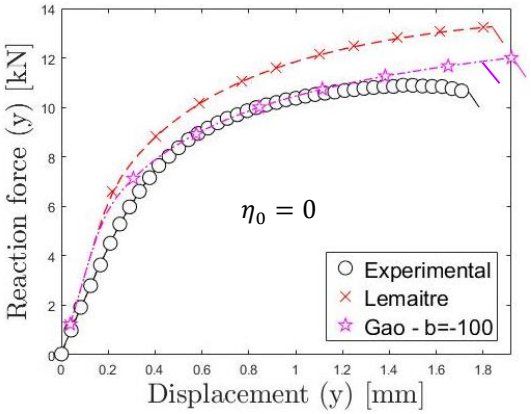

b) Reaction curve - AISI 4340 normalized

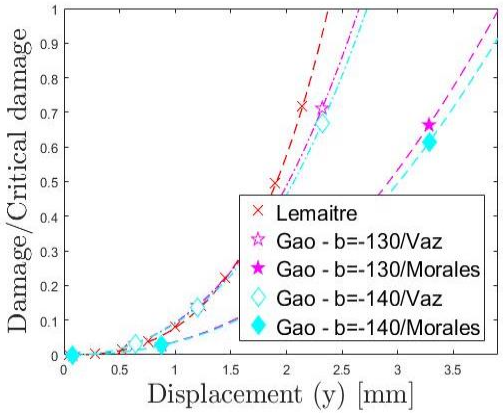

c) Evolution of damage AISI 4340 annealed

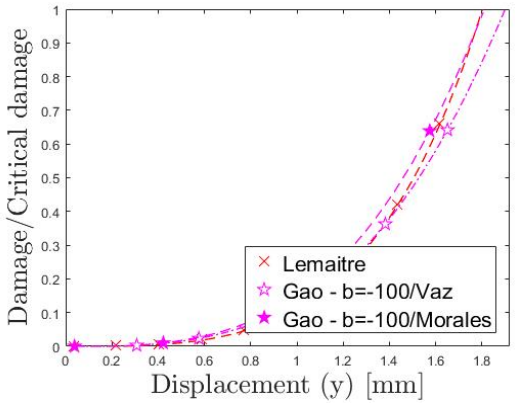

d) Evolution of damage AISI 4340 normalized

Figure 3: Results pure shear specimens.

Figure 4 (a) and Figure 5 (a) shows the region in which the failure of the specimen after the experimental test. The contours of the damage distribution indicate a high concentration on the face of specimens, in the middle of the thickness, which corresponds to the fracture zone, therefore, the specimen subjected to pure shear loading presents its failure in the center of the critical region. For the annealed alloy, this phenomenon can be seen in Figures 4 (b), (c), (d), (e) and (f). For the normalized alloy, the contours of the damage distribution can be viewed in Figure 5 (b), (c) and (d). According to the results presented, it is possible to affirm that the prediction of the correct fracture location for both annealed and normalized material presents a good approximation when using the fracture indicator coupled to the Gao model.

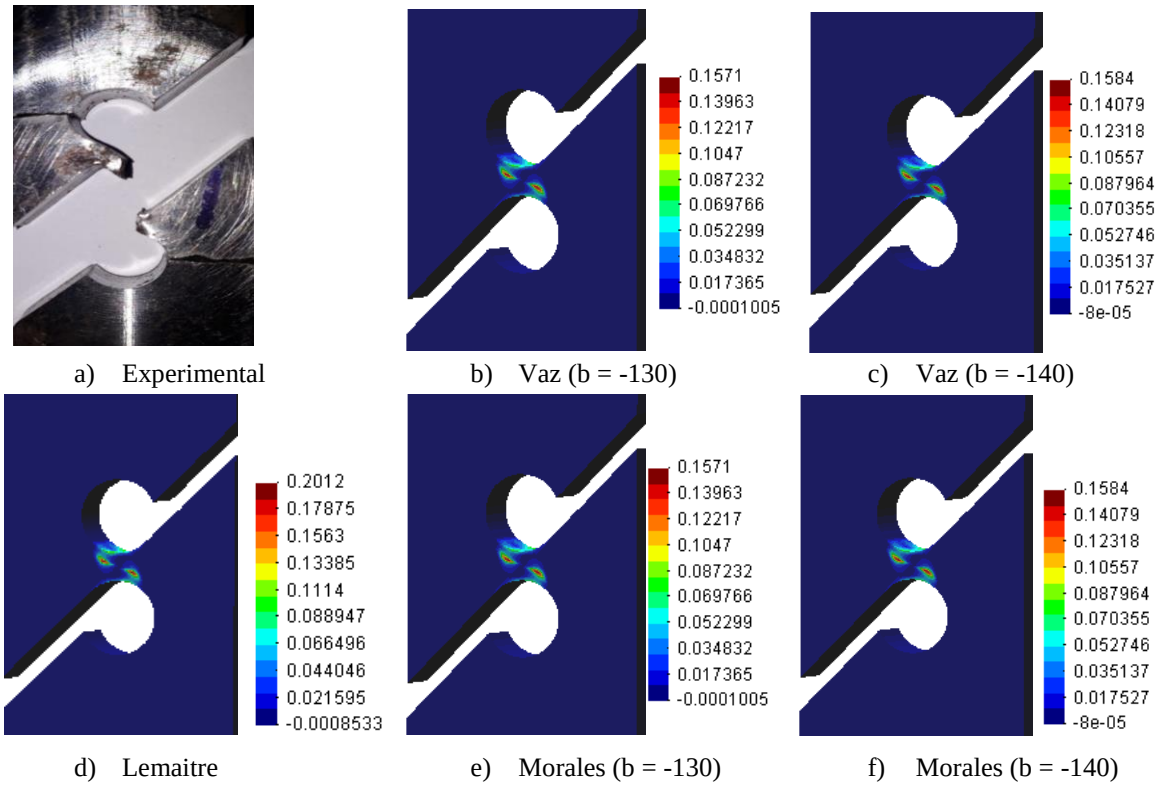

a) Experimental b) Vaz (b = -130) c) Vaz (b = -140)

d) Lemaitre e) Morales (b = -130) f) Morales (b = -140)

Figure 4: Contour of the damage parameter for pure shear specimens - AISI 4340 annealed

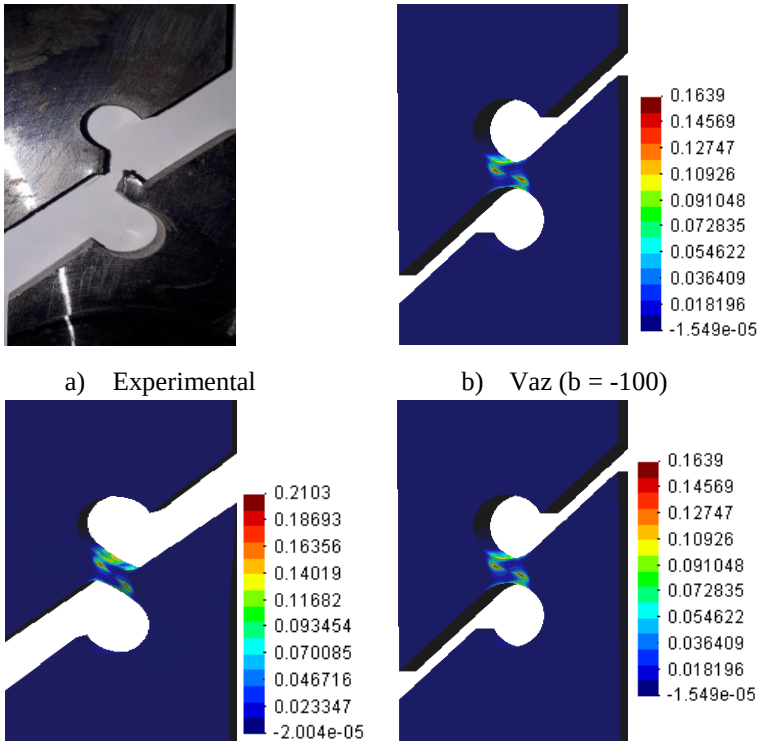

a) Experimental b) Vaz (b = -100)

c) Lemaitre d) Morales (b = -100)

Figure 5: Contour of the damage parameter for pure shear specimens - AISI 4340 normalized

6 CONCLUSION

The new ductile fracture indicator allows predicting the correct fracture location of materials, with different levels of ductility, as well as obtaining the levels of reaction forces using the damage indicator coupled to the yield function in the Gao model, in the post-processing step. The results show a significant improvement in predicting the exact point at which failure occurs. This means that it is possible to approximate fracture displacement, both for loading conditions, at the calibration point, and for situations outside this point. The reaction force is also estimated much more accurately when comparing the predictions of the Gao and Lemaitre models.

ACKNOWLEDGEMENTS

The authors acknowledge the Faculty of Engineering Science and the Institute of Industrial Design and Methods of the Austral University of Chile for financial support for this publication. Lucival Malcher would like to acknowledge the support from the Brazilian Council for the Scientific and Technological Development - CNPq (contract 311933/2018-1).

REFERENCES

[1] Khan, A S, Huang, S. (1995). *Continuum Theory of Plasticity*. Houston, Texas: Jhon Wiley.

[2] Brünig, M., Chyra, O., Albrecht, D., Driemeier, L., Alves, M. (2008). A ductile damage criterion at various stress triaxialities. International Journal of Plasticity, 1731-1755.

[3] Gao, X., Roe, C. (2010). A Study on the Effect of the Stress State on Ductile Fracture. International Journal of Damage Mechanics, DOI: 10.1177/1056789509101917.

[4] Gao, X., Zhang, T., Zhou, J., Graham, S.M., Hayden, M., Roe, C. (2011). On Stress-state dependent plasticity modeling: Significance of the hydrostatic stress, the third invariant of stress deviator and the non-associated flow rule. International Journal Plasticity, 217-231.

[5] Malcher, L., Andrade Pires, F. M., César De Sá, J. M. A. (2012) An assessment of isotropic constitutive models for ductile fracture under high and low stress triaxiality. International Journal of Plasticity, v. 30-31, p. 81-115.

[6] Bao, Y. (2003). Prediction of Ductile Crack Formation in Uncracked Bodies. Cambridge/Massachusetts: MIT.

[7] Bai, Y. (2008). Effect of Loading History on Necking and Fracture. Cambridge/ Massachussetts: MIT.

[8] Chaboche, J. L. (1988). Continuum Damage Mechanics: Part I - General Concepts. Jounal of Applied Mechanics, 59-64.

[9] Lemaitre, J., & Desmorat, R. (2005). *Engineering damage mechanics: ductile, creep, fatigue and brittle failures*. Springer: New York.

[10] Vaz Jr. M., Owen, D. R. J. (2001). Aspects of ductile fracture and adaptive mesh refinemnt in damaged elasto-plastic materials. International Journal for Numerical Methods in Engineering, 29-54.

[11] Lemaitre, J. (1985). A Continuous Damage Mechanics Model for Ductile Fracture. Journal of Engineering Materials and Technology, 83-89.

[12] Driemeier, L., Moura, R.T., Machado, I.F., Alves, M. (2015). A bifailure specimen for accessing failure criteria performance. International Journal of Plasticity, 62-86.

[13] Brünig, M., Gerke, S., Schmidt, M. (2016). Biaxial experiments and phenomenological

modeling of stress-state-dependent ductile damage and fracture. International Journal of Fracture, 63-76.

[14] Gerke, S., Adulyasak, P., Brünig, M. (2017). New biaxially loaded specimens for analysis of damage and fracture in sheet metals. International Journal of Solids and Structures, 209-218.

[15] Yan, S., Zhao, X. (2018). A fracture criterion for fracture simulation of ductile metals based on micromechanisms. Theoretical and Applied Fracture Mechanics, 127-142.

[16] Haji Aboutalebi, F., Poursina, M., Nejatbakhsh, H., Khataei, M. (2017). Numerical simulations and experimental validations of a proposed ductile damage model for DIN1623 St12 steel. Engineering Fracture, 276-289.

[17] Farahani, B.V., Belinha, J., Amaral, R., Tavares, P.J., Moreira, P. (2018). A digital image correlation analysis on a sheet AA6061-T6 bi-failure specimen to predict static failure. Engineering Failure Analysis, 179-196.

[18] Brünig, M., Gerke, S., Schmidt, M. (2018). Damage and failure at negative stress triaxialities: Experiments, modeling and numerical simulations. International Journal of Plasticity, 70–82.

[19] Brünig, M., Zistl, M., Gerke, S. (2019). Biaxial experiments on characterization of stress state dependent damage in ductile metals. German Academic Society for Production Engineering (WGP), https://doi.org/10.1007/s11740-019-00930-2.

[20] Brünig, M. (2019). *Continuum Damage Model for Ductile Materials Based on Stress-State-Dependent Damage Functions*. Em A. Ö. H. Altenbach, Encyclopedia of Continuum Mechanics (pp. doi.org/10.1007/978-3-662-53605-6_253-1). Germany: Springer-Verlag GmbH.

[21] Malcher, L., Mamiya, E. N. (2014). An Improved Damage Evolution Law Based on Continuum Damage Mechanics and its Dependence on Both Stress Triaxiality and the Third Invariant. *International Journal of Plasticity, 56*, 232-261.

[22] Sun, S., Liu, Q., Brandt M., Luzin, V., Cottam, R., Janardhana, M., Clark, G. (2014). Effect of laser clad repair on the fatigue behaviour of ultra-high strength AISI 4340 steel. Materials Science & Engineering A 606, 46–57.

[23] Simo, J. C., Hughes, T. J. (1998). *Computational Inelasticity*. New York: Springer-Verlag.

[24] De Souza Neto, E. A., Peric, D., Owen, D., R., J. (2008). *Computational methods for plasticity: theory and applications.* Singapura: John Wiley & Sons Ltd.

[25] Kleinermann, J. P.; Ponthot, J. P. (2003). Parameter identification and shape/process optimization in metal forming simulation. Journal of Materials Processing Techonology, pp. 521-26.